Ocean Engineering 283 (2023) 115007

Contents lists available at ScienceDirect

Ocean Engineering

journal homepage: www.elsevier.com/locate/oceaneng

Wave inhomogeneities in a wave basin of constant water depth

Sébastien Laflèche [a,b,*], Babak Ommani [b], Trygve Kristiansen [b], Sébastien Fouques [a]

[a] SINTEF Ocean, Trondheim, 7050, Norway
[b] Department of Marine Technology, NTNU, Jonsvannsveien 82, Trondheim, 7050, Norway

ARTICLE INFO

Keywords:
Wave homogeneity
3D wave basin
Numerical wave basin
Wave generation
Optimization

ABSTRACT

Experimental testing of large marine structures in hydrodynamic laboratories requires an accurate reproduction of waves over a large area of the basin. However, with a uniform motion of the wavemaker, wave interactions with the basin's boundaries can result in an inhomogeneous wave field, even before beach reflection takes place. In this paper, the main geometrical parameters causing inhomogeneities are investigated. For that purpose, a fast linear model is implemented and applied to describe wave fields in basins of arbitrary geometry but constant water depth. Comparisons with experiments in SINTEF's Ocean Basin demonstrate the validity of the model for regular waves. Finally, an efficient method to reduce wave field inhomogeneities by optimizing the motion of the paddles of a multiflap wavemaker is presented and validated experimentally.

1. Introduction

Model testing continues to be an unavoidable tool in investigating the behaviour of floating structures in the ocean, even though the use of numerical simulations is constantly growing as they always become more accurate and less time-consuming. Among other reasons, this is particularly true when introducing new and complex structural designs. An example of such new designs is large structures such as floating bridges, that cover large areas and are sensitive to variations of wave parameters across their length. Indeed, Cheng et al. (2018) have shown that the variability of wave conditions across the pontoons of an end-anchored curved floating bridge has a significant effect on the motions and the moments in the structure. Dai et al. (2021) added that for the same type of bridge, inhomogeneity of the wave field strongly affects fatigue damage of mooring lines. In addition to floating bridges, other examples of structures covering large areas include arrays of wave energy converters (Rodrigues, 2021), aquaculture farms, floating solar islands, or offshore wind farms. Unlike conventional designs, testing of such large structures requires an accurate reproduction of waves not only in the centre of the basin, but over a large area. Therefore, for such tests, the notion of wave field homogeneity is of critical importance. Herein, we define an inhomogeneous wave field as a wave field for which wave statistics, including the directional spectrum, vary in space.

Analytical expressions of transfer functions for waves generated by wavemakers have long been established. However, they exist only for specific basin geometries. They were first derived within the assumption of two-dimensional wave propagation, both at first order (Biésel and Suquet, 1951), and at second order (Schäffer, 1996). The theory was extended to directional waves at second order, but for a basin of infinite horizontal extend with infinitely wide wavemakers (Schäffer and Steenberg, 2003). However, most ocean basins have more complex geometries: the wavemaker has a finite width, and because of the lateral boundary conditions, the wave field becomes inhomogeneous.

A common design for rectangular ocean basins is to have one wavemaker with a vertical wall on both sides. The length of the wavemaker becomes virtually infinite in this design, which is theoretically ideal for simply propagating waves (Dalrymple, 1989). However, transverse sloshing modes can then appear, and waves scattered by the model to be tested can also be reflected by the side walls. Thus, another common design is to have wavemakers on two adjacent sides and beaches on the opposite sides. The purpose of the beaches is to absorb waves generated by the wavemakers, as well as those reflected by the model to be tested. Replacing a side wall with a beach has another effect: it results in the diffraction of the incident wave, leading to an additional three-dimensional wave pattern. This affects the homogeneity of the wave field in the whole basin and restricts the working area (Gilbert and Huntington, 1991).

For a wavemaker of finite width in an infinite basin – or equivalently for a basin with perfect wave absorbers on both sides of the wavemaker – Matsumoto and Hanzawa (1996) have shown that homogeneity of the wave field could be improved with a multiflap wavemaker by having a non-uniform distribution of the flaps' motion. They solved analytically the 2D Helmholtz equation in their domain, and validated

* Corresponding author at: SINTEF Ocean, Trondheim, 7050, Norway.
E-mail addresses: sebastien.lafleche@sintef.no (S. Laflèche), babak.ommani@ntnu.no (B. Ommani), trygve.kristiansen@ntnu.no (T. Kristiansen), sebastien.fouques@sintef.no (S. Fouques).

https://doi.org/10.1016/j.oceaneng.2023.115007
Received 7 February 2023; Received in revised form 24 May 2023; Accepted 30 May 2023
Available online 19 June 2023

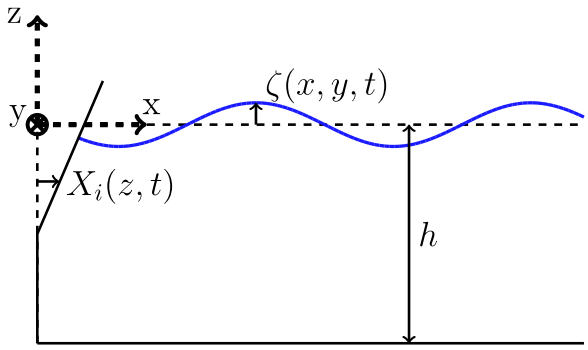

Fig. 1. Definition of the Cartesian coordinate system and main quantities.

the method experimentally. O'Dea and Newman (2007) confirmed those results, studying various 3D wavemakers using WAMIT® (WAMIT Inc., 2020). Ota et al. (2021) used a similar technique, but with time-dependent Green functions, to study a basin with wavemakers installed along the whole perimeter.

O'Boyle et al. (2017) worked on optimizing the shape of the transition walls between the wavemaker and the side beaches of their shallow-water basin. Their target was to find a compromise between absorbing waves radiated by the tested model, and diffraction of the incident waves. They used a combination of experiments and numerical modelling using Boussinesq equations.

The homogeneity of the wave field in SINTEF's Ocean Basin was documented experimentally by Rabliås and Kristiansen (2022) for long-crested regular waves in deep water. In the case of long-crested regular waves, the definition of a homogeneous wave field becomes having a uniform wave direction and amplitude across the area of interest. Measuring free-surface elevation across the whole basin, discrepancies of up to 30% of wave amplitude were observed exhibiting clear interference patterns.

This paper investigates the sensitivity of wave field homogeneity to geometrical details of ocean basins, and proposes a method to reduce the wave field inhomogeneities. An efficient Green-function method for wave propagation in basins of constant water depth with complex geometries is presented, extending the formulation of Barailler and Gaillard (1967) and Nishimura et al. (1994). The method solves analytically the depth-dependency of the velocity potential, thus allowing to solve directly for the free-surface elevation in a two-dimensional domain. This greatly reduces the computational complexity of the problem compared to 3D BEM solvers. Results obtained with this model are systematically compared with the experiments of Rabliås and Kristiansen (2022). Moreover, it is used to investigate the cause of those inhomogeneities, as well as their consequences on model tests. Further, a correction method to improve wave field homogeneity is proposed. New experiments have been conducted for the present article in SINTEF Ocean's basin during the summer of 2022, with regular waves of various periods and steepnesses, in order to validate the method and quantify its effect.

2. Numerical method

A panel method code was developed and adopted to solve for the free-surface elevation in an Ocean basin, using linear potential flow theory. Assumptions behind the model and its principle are presented in this section, as well as two verification cases.

2.1. Formulation of the problem

The problem here is to find the free-surface elevation $\zeta(x,y,t)$ and the velocity potential $\Phi(x,y,z,t)$ in a three-dimensional basin, given the displacement of each flap of a wavemaker with N flaps, $X_i(z,t)$, where $i \in [\![1,N]\!]$. In the present article, wavemaker refers to the entire wave machine, while flap is used to refer to an individual wave paddle. The coordinate system is taken so that z is positive upwards (see Fig. 1). For the purpose of the present numerical model, the following assumptions are made:

- Linear potential flow theory (incompressible and inviscid fluid, low wave steepness and small paddle motion)
- Uniform water depth h
- Rapidly decaying evanescent modes (as described below) are neglected

As linear potential flow theory is assumed, the problem can be solved for a given wave frequency, and the contributions of all frequency components summed afterwards. The formulation will be presented for a given angular frequency ω. The complex free-surface elevation can then be written $\zeta(x,y,t) = \eta(x,y)e^{-i\omega t}$. For a constant water depth h, η satisfies a 2D Helmholtz equation (Mei et al., 2005):

$$(\Delta + k^2)\eta = 0 \tag{1}$$

where Δ is the 2D Laplacian with respect to (x,y), k is a solution of the linear dispersion relationship $\omega^2 = gk\tanh(kh)$, and g is the acceleration of gravity. An infinity of complex solutions k_j exists for the wavenumber, each one associated with wave components following a different Helmholtz equation. There is however only one real solution of the dispersion relationship: let it be k_0. All the other solutions are imaginary, and for them, $\forall j \geq 1, |k_j| > \frac{\pi}{2h}$. Thus, solutions of the Helmholtz equation associated with an imaginary wavenumber are rapidly decaying evanescent modes, decreasing faster than $\exp\left(-\frac{\pi x}{2h}\right)$, and will be neglected here. Because of this rate of decay, those modes are only present within a distance of the wavemaker smaller than twice or three times the water depth, and neglecting them does not affect results beyond this limit. Then, the free-surface elevation is solution of the 2D Helmholtz equation:

$$(\Delta + k_0^2)\eta = 0 \tag{2}$$

The boundaries of the basin can be either wavemakers, vertical walls, or wave absorbers. Even though the model detailed here can include partial directional reflection, all wave absorbers will be considered perfectly absorbing for this study.

For a perfectly absorbing wave absorber, a radiation condition has to be enforced. This condition is the same as for an infinite basin in the horizontal direction. Thus, perfectly absorbing boundaries can be equivalently replaced by openings into an infinite domain, where a radiation condition is enforced at infinity. This property is used for all such boundaries.

Walls and wavemakers have the same linear impermeability condition, $\partial_n \Phi = \partial_t X$, where X is the displacement of the flap, ∂ indicates a partial derivative, and $\underline{n}$ is the normal to the boundary, oriented towards the fluid. As the problem is written in terms of free-surface elevation, all boundary conditions should also be rewritten in terms of free-surface elevation. For a wall, $X = 0$, and the condition simply becomes $\partial_n \eta = 0$. For a wavemaker, some additional steps are necessary, and the derivations will be presented in Section 2.2.2.

If velocities or accelerations are of importance, then the velocity potential can be derived back from the free-surface elevation, as

$$\Phi = \frac{-ig}{\omega}\frac{\cosh(k_0(z+h))}{\cosh(k_0 h)}\eta e^{-i\omega t} \tag{3}$$

2.2. Numerical model

2.2.1. Principle of the panel method

To obtain the solution for the free-surface elevation η, the problem is reformulated using a boundary integral method, by introducing a distribution of sources and dipoles along the physical boundaries of

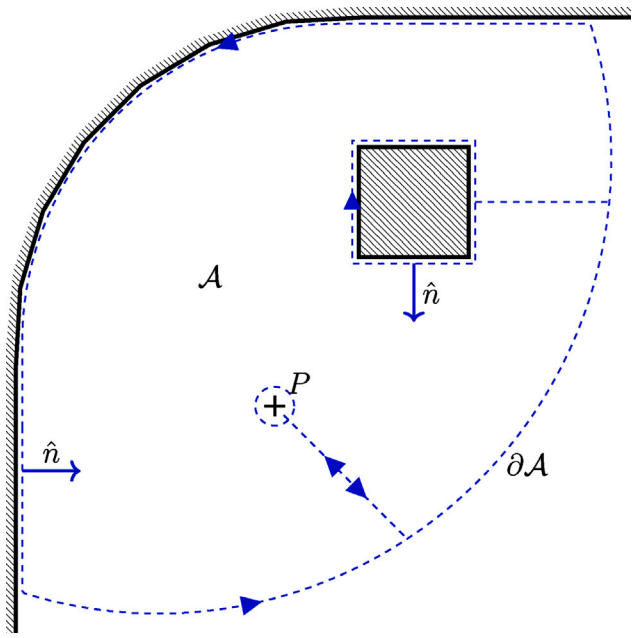

Fig. 2. Definition of the domain for the boundary value problem.

the domain, as shown in Fig. 2. If the domain is unbounded, then its boundary $\partial\mathcal{A}$ has to extend to infinity. The boundaries are later discretized using a lowest-order boundary element method. As the equation to be solved is the Helmholtz equation on a 2D domain, the panels that are distributed along its boundaries are 1D. The Green function for the Helmholtz equation satisfying Sommerfeld's radiation condition at infinity is given for a source $\underline{P}$ and a point $\underline{Q}$ by

$$G_P(\underline{Q}) = -\frac{i}{4} H_0^{(1)}(k_0 r) \tag{4}$$

where $r(\underline{P}, \underline{Q}) = |\underline{Q} - \underline{P}|$, and $H_0^{(1)}$ is the zeroth-order Hankel function of the first kind (Sommerfeld, 1949).

An expression of the free-surface elevation is then obtained by Green's theorem:

$$\eta(\underline{P}) = \int_{\partial\mathcal{A}} \left[\eta(\underline{Q})\nabla G_P(\underline{Q}) \cdot \hat{n} - G_P(\underline{Q})\partial_n\eta(\underline{Q})\right] ds \tag{5}$$

As for perfectly reflecting walls, $\partial_n\eta = 0$, they are described as distributions of dipoles only. Wavemakers that are not on a symmetry axis are still described by a distribution of both sources and dipoles. Compared to the method derived in Barailler and Gaillard (1967) and Nishimura et al. (1994), wavemakers are part of the boundary, so that no explicit incident wave field is needed. Moreover, the domain here does not need to be convex, and can include internal walls, as shown in Fig. 2.

Panels of finite length Δs with constant source and dipole strengths are considered. Let W_i be a panel, and $\underline{P_i}$ its centre. Assuming that the length of the panel is $\Delta s_i \ll \lambda = \frac{2\pi}{k_0}$, the approximation $\forall \underline{Q} \in W_i, \eta(\underline{Q}) = \eta(\underline{P_i})$ is then made. The contribution η_i^d from the panel W_i to the free-surface elevation is then:

$$\eta_i^d(\underline{P}) = \eta(\underline{P_i}) \int_{W_i} \partial_{n_i} G_P ds - \partial_{n_i}\eta(\underline{P_i}) \int_{W_i} G_P ds \tag{6}$$

However, Eq. (6) is only valid for $\underline{P} \notin W_i$. Thus, $\eta_i^d(\underline{P_i})$ will be taken as the limit of $\eta_i^d(\underline{P})$ for $\underline{P}$ approaching $\underline{P_i}$ normally to the panel. This yields:

$$\lim_{\underline{P}\to\underline{P_i}} \eta_i^d(\underline{P}) = \frac{\eta(\underline{P_i})}{2} - \partial_{n_i}\eta(\underline{P_i}) q\left(\frac{\Delta s_i}{2}, k_0\right) \tag{7a}$$

where:

$$q(\delta, k_0) = \frac{1}{2ik_0} \int_0^{k_0\delta} H_0^{(1)} \tag{7b}$$

For points a few panel lengths away from the panel, the contribution from the panel W_i is considered to be similar to a single source or dipole placed in its centre, $\underline{P_i}$. If there are one or two orthogonal infinite walls, then symmetry can be used instead of placing panels on those walls.

The contribution from a panel i on a point $\underline{P}$ is then:

$$\eta_i^d(\underline{P}) = \sigma_i G_{P_i}(\underline{P}) + 2\gamma_i \partial_{n_i} G_{P_i}(\underline{P}) \tag{8a}$$

where:

$$\gamma_i = \left[\sum_{j\neq i} \eta_j^d(\underline{P_i}) - \partial_{n_i}\eta(\underline{P_i}) q\left(\frac{\Delta s_i}{2}, k_0\right)\right] \Delta s_i \tag{8b}$$

$$\sigma_i = -\partial_{n_i}\eta(\underline{P_i})\Delta s_i \tag{8c}$$

To compute $q(\delta, k_0)$, as $\forall i, k_0\Delta s_i \ll 1$, the following expansion has been used, obtained by integration from Abramowitz and Stegun (1964):

$$\begin{aligned}\int_0^x H_0^{(1)} =& x + \frac{2i}{\pi}\left[\ln\left(\frac{x}{2}\right) + \gamma - 1\right] x - \frac{x^3}{12} \\ &- \frac{i}{6\pi}\left[\ln\left(\frac{x}{2}\right) + \gamma - \frac{4}{3}\right] x^3 + \mathcal{O}(x^4)\end{aligned} \tag{9}$$

Only $\underline{\gamma} = \left(\cdots \gamma_i \cdots\right)^T$ is still unknown here. Using (8) to evaluate every γ_i yields a system of equations:

$$\mathbb{G}\underline{\gamma} = \underline{\eta}^I \tag{10a}$$

where:

$$(\mathbb{G})_{ij} = \begin{cases} -\partial_{n_j} G_{P_j}(\underline{P_i})\frac{\Delta s_i}{2}, & \text{if } i \neq j \\ 1, & \text{if } i = j \end{cases} \tag{10b}$$

$$(\underline{\eta}^I)_i = \sum_{j\neq i} \sigma_j G_{P_j}(\underline{P_i})\Delta s_i + \sigma_i q\left(\frac{\Delta s_i}{2}, k_0\right) \tag{10c}$$

Having found $\underline{\gamma}$, Eq. (8) is then used to find the free-surface elevation at any point of the basin.

2.2.2. Source strength

At a wavemaker, an impermeability condition applies: the normal speed of water particles follows that of the wavemaker. This condition gives the source strength $\sigma = -\partial_n\eta\Delta s$. It should be noticed that both propagative and evanescent modes are generated. Evanescent modes can have two different origins. Some exist also in two-dimensional basins, that appear because the wavemaker's vertical profile does not equal that of the velocity profile of a freely propagating wave. Those modes are all rapidly decaying and are the ones that will be neglected. Other evanescent modes appear in three-dimensional basins, and are due to lateral variations of the wavemaker motion (flaps of finite width, or finite length of the wavemaker for instance). Those modes can decay slowly, and are intrinsically part of the solution computed by the present numerical model. The contribution of the propagative and the second type of evanescent modes on $\partial_n\eta$ can be isolated by taking the projection of the boundary condition onto the mode $z \mapsto \cosh\left(k_0(z+h)\right)$. Let the horizontal displacement of a flap be $X(z,t) = X_a S(z) e^{-i\omega t}$, where S is a vertical profile, and X_a is the amplitude of the flap displacement. Then, the projected boundary condition yields:

$$\partial_n\eta = X_a k_0 c_0 \tag{11}$$

where c_0 is the Biésel transfer function (Biésel and Suquet, 1951):

$$c_0 = \sinh(k_0 h) \frac{\int_{-h}^0 S(z)\cosh k_0(z+h) dz}{\int_{-h}^0 \cosh^2 k_0(z+h) dz} \tag{12}$$

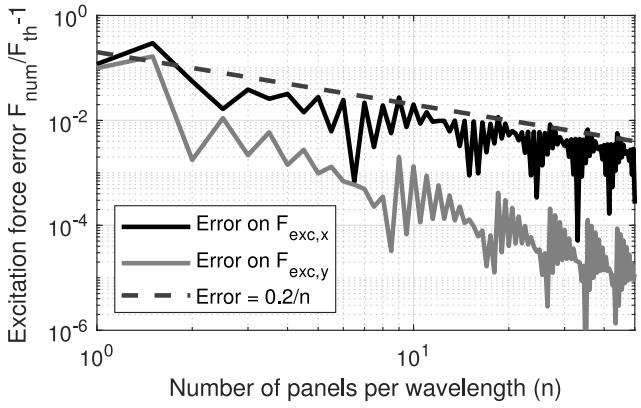

Fig. 3. Convergence study on the excitation force from a regular long-crested wave on a bottom mounted vertical cylinder – $T = 1.5$ s, $D = 10$ m, $h = 5$ m – F_{num} and F_{th} being the excitation forces obtained respectively numerically and theoretically.

2.2.3. Partial and directional reflection

In addition to considering perfectly reflecting or absorbing walls or beaches respectively, the present method allows for considering partial reflection. This can be done to a first approximation by multiplying the dipole strengths with a known reflection coefficient $R(\omega)$, whose phase has then to be set to consider the phase of the reflected wave. The directionality of the reflection can also be included. To this end, a simplification can be made by considering that the contribution from each panel is locally a long-crested wave coming from a given angle, and then multiplying the contribution of each one of those panels by $R(\omega, \theta)$ in the expression of γ_i in Eq. (8). Using this feature to model reflections is left for future studies, and the method is not used in this article, as the goal here is to describe the wave field before reflection from the beaches reaches the wave probes.

2.3. Verification

Verification of the numerical solver is done on two test cases where analytical solutions exist.

2.3.1. Free-surface diffraction from a cylinder

Simulation results for the diffraction of an incident long-crested wave by a vertical, surface-penetrating circular cylinder standing on a flat seabed were compared to the analytical solution of MacCamy and Fuchs (1954). Panels with dipoles were placed along the border of the circular cylinder. The width of each panel was taken as $\Delta s = \lambda/n$, where λ is the wavelength of the incident wave at the frequency of interest, and n is the number of panels per wavelength.

The excitation force on the cylinder was computed by direct pressure integration from the numerical solution. For a wall, the integrated force on a panel $\underline{F_i}$ can be directly found from the dipole strength

$$\underline{F_i} = 2\gamma_i \hat{n}_i \times \rho g \int_{-h}^{0} \frac{\cosh(k_0(z+h))}{\cosh(k_0 h)} dz e^{-i\omega t} \tag{13}$$

where $\hat{n}_i$ is the normal to the panel i. The excitation force F_{exc} is then obtained by summing the contribution of the forces on each panel. Results converge towards the theoretical solution (see Fig. 3). The order of convergence is first order, which is consistent with our lowest-order panel method. For the wave field, it can also be seen that the numerical solution converges towards the analytical one (see Fig. 4).

As the panels are 1D, even with a dense mesh, simulations remain fast. Hence, a first-order convergence speed was deemed acceptable. $n = 20$ panels per wavelength were used in the simulations performed in the following.

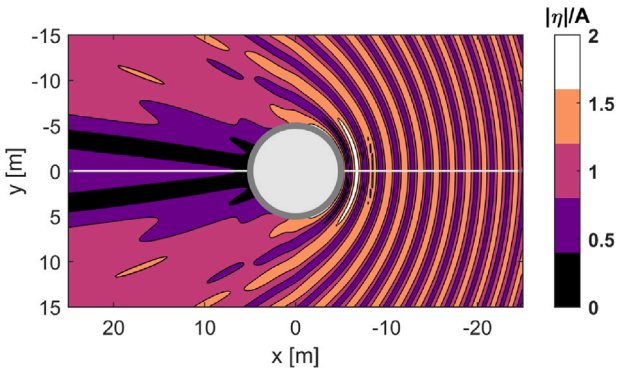

Fig. 4. Comparison of theoretical (top-half) and numerical (bottom-half) solutions for a regular long-crested wave diffracted by a vertical cylinder extending all the way to the seabed – $T = 1.5$ s, $D = 10$ m, $h = 5$ m.

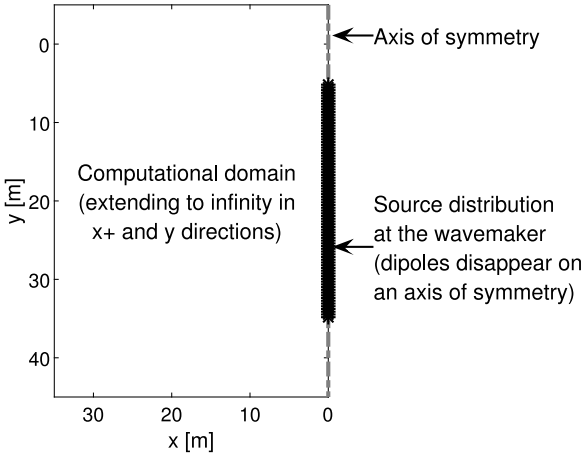

Fig. 5. Definition of the numerical domain for modelling waves generated by a finite wavemaker – Wavemaker at $x = 0$ m with a width of $l_p = 30$ m.

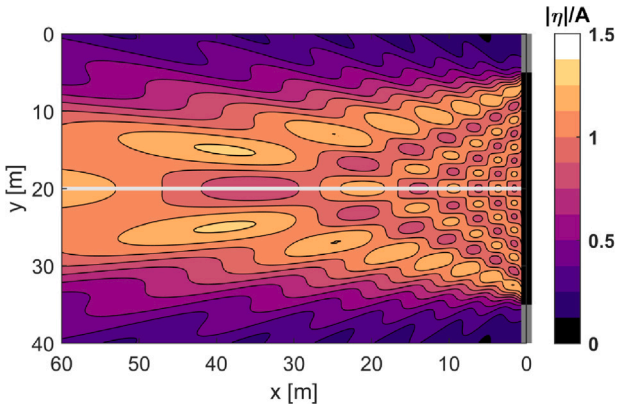

Fig. 6. Comparison of theoretical (top-half) and numerical (bottom-half) wave amplitudes for a wave generated by a finite wavemaker (black line at $x = 0$ m, on a wall represented by the grey line) in an infinite basin in the x+ and y directions – $T = 1.5$ s, $h = 5$ m.

2.3.2. Waves from a finite wavemaker

The wave field generated by a finite wavemaker of width l_p in an infinitely wide basin was also used to compare results from the simulation to an analytical solution (see Fig. 5 and Fig. 6). The wavemaker boundary condition here is $\partial_x \eta_{|x=0} = X_a k_0 c_0 \text{rect}\left((y - y_0)/l_p\right)$: a rectangle function centred on $y = y_0$, with discontinuities on both sides. The analytical solution was derived using a Fourier transform in y of the

boundary condition, and solving for each mode thus obtained, similarly to what is done by Dalrymple (1989). This gives

$$\begin{aligned}\eta(\underline{X}) &= \int_{-\infty}^{\infty} \frac{1}{ik_x} \mathcal{F}\left(\partial_x \eta_{|x=0}\right) e^{i\underline{k}.\underline{X}} dk_y \\ &= \frac{X_a k_0 c_0 l_p}{2\pi} \int_{-\infty}^{\infty} \frac{e^{-ik_y y_0}}{ik_x} \operatorname{sinc}\left(\frac{k_y l_p}{2}\right) e^{i\underline{k}.\underline{X}} dk_y\end{aligned} \tag{14}$$

where $\underline{X} = (x, y)^T$ is any point in the domain, $\mathcal{F}$ is the Fourier transform in y, $k_x = \sqrt{k_0^2 - k_y^2}$ and $\underline{k} = \left(k_x, k_y\right)^T$. For the numerical solution, a symmetry condition was used to describe the effect of the perfectly reflecting and infinite wall on which the wavemaker is located. The domain, as presented in Fig. 2, extends to infinity. If one of the walls that extend to infinity is not on an axis of symmetry, then it needs to be approximated by a wall of finite length. In this case, the solution slightly differs from the theory, but approaches it as the width of the wall increases. For this case also, the numerical solution matches the analytical one (see Fig. 5).

Oscillations in wave amplitude can be observed along the wavemaker, even far from its extremities. As those oscillations appear not only in the numerical, but also in the theoretical solution, they are not due to numerical errors. As wave components decay if $|k_y| > k_0$, wave propagation in the x-direction acts as a low-pass filter, and an effect similar to the Gibbs phenomenon appears (Wilbraham, 1848). It explains why the characteristic length of those oscillations has a scale similar to that of the wavelength. If the boundary condition had directly applied to the free-surface elevation $\eta_{|x=0}$, then the wave amplitude would be uniform right in front of the wavemaker, and oscillations due to the Gibbs phenomenon would gradually appear further away from the wavemaker, as the evanescent modes decay. However, as the boundary condition applies on $\partial_x \eta_{|x=0}$ and not directly on $\eta_{|x=0}$, oscillations of $|\eta|$ can be found even close to the wavemaker. The larger the wavemaker is compared to the wavelength, the smaller the amplitude of the oscillations at the centre of the wavemaker is.

2.4. Numerical simulations

Simulations were run with a standard personal laptop (AMD Ryzen™ 5 3550H CPU, 16 GB RAM), using MATLAB® (MATLAB, 2022). For an array of 24 by 20 points, and $n = 20$ panels per wavelength, for $T = 1.5$ s, the simulation takes 0.05 s. For the optimization process presented in Section 5, for 143 flaps and an array of 50 × 30 optimization points, the simulation takes on average 5 s.

3. Experimental setup

3.1. Description of the basin

Two series of experiments were run in the Ocean basin at SINTEF Ocean. The first one was conducted in 2018 by Rabliås and Kristiansen (2019, 2022), and brought to light the presence of inhomogeneity patterns in the wave field. The second was conducted in 2022 by the authors, for the present article, in order to evaluate a correction method for those inhomogeneities. The basin is about 60 m by 50 m (not including the beaches), with wavemakers on two sides. One of them is a double-hinged flap wavemaker ("BM2" in Fig. 7), and the other one is a single-hinged multiflap wavemaker with 143 flaps, each 43 cm wide ("BM3" in Fig. 7). On the two other sides, parabolic beaches act as wave absorbers. All dimensions are presented in Fig. 7. For the experiments, a constant water depth of 5 m was used.

As the study focuses on waves before reflection, in the numerical model of the basin, both beaches are considered perfectly absorbing.

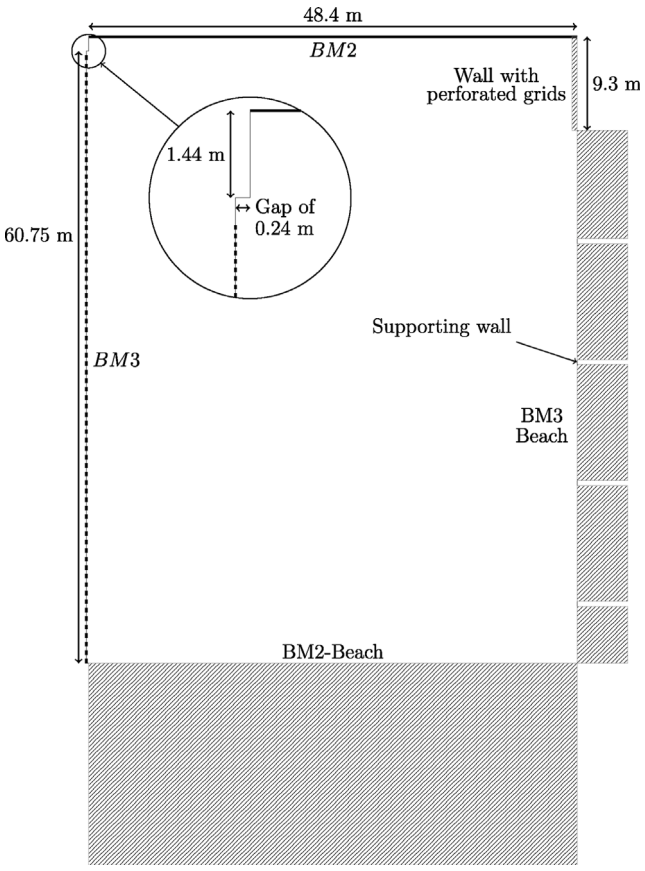

Fig. 7. Dimensions of SINTEF's Ocean basin used for the experiments — BM2 and BM3 indicating respectively the single-flap and the multi-flap wavemakers.

3.2. Instrumentation and test program

Wave measurements were performed with a rectangular wave probe array, composed of probes separated by a distance of around 2 meters (4 by 5 probes on a grid of 2 m by 2 m in the first test campaign, 3 by 4 probes on a grid of 2.17 m by 2.45 m in the second one), and a small circular array used to measure directional properties of waves. Each wave was then repeated several times, moving the wave probe arrays between each repetition, in order to map a large area of the basin. The free surface was brought to rest between tests.

In the first test campaign, five regular long-crested waves were run, at different wave periods, with the double-hinged flap wavemaker BM2 (see Table 1). Some results are presented in Section 4. As the implementation of a correction requires a multiflap wavemaker, it is the other wavemaker, BM3, which was used in the second test campaign. Both the description of the correction method and the results are presented in Section 5. The correction was tested for two wave periods and two wave steepnesses (see Table 2). The steepness is characterized by H/λ, where H is the wave height and λ is the wavelength. The correction was also compared to a correction appropriate for an infinitely wide basin, similar to the already existing correction methods (Matsumoto and Hanzawa, 1996).

In order to quantify repeatability errors, one specific wave was repeated 18 times during the test campaign, while leaving the wave probe array at the same position. This test wave was repeated at least twice per day for the full duration of the test campaign. Repeatability errors on the amplitude of free-surface elevation were less than ±2% (the uncertainty here includes both that in the measurements, and in the generated wave).

Table 1
Test program for the first test campaign (Rabliås and Kristiansen, 2022).

Period [s]	Wave steepness (H/λ)
1.00	1/38
1.25	1/41
1.50	1/32
1.75	1/39
2.00	1/38

Table 2
Test program for the second test campaign.

Period [s]	H/λ	Correction
1.5	1/45	With, without, and simple correction
2.0	1/45	With, without, and simple correction
1.5	1/20	With and without
2.0	1/20	With and without

3.3. Data processing

In order to describe inhomogeneity patterns, the investigated quantity here is the difference between the measured amplitude of the basic harmonic component of the wave and the specified target amplitude. This difference, in percentage, is referred to as the deviation from the target amplitude. Measurements of amplitudes are taken after a steady state is reached, but before reflection from the beach reaches the wave probes.

The time window thus defined is a function of the position of the probe. More precisely, for a wavemaker at $x = 0$ m, it is a function of the x-coordinate of the probe. A first estimate of the time window at a given x is obtained from linear theory. The wavemaker motion starts with a ramp in time. Propagating this ramp, assuming that the wave is two-dimensional, gives a first estimate of when the steady state is first reached (grey line in Fig. 8). On the beach facing the wavemaker, the wave is progressively reflected. Assuming that the wavefront propagates at the group velocity, and considering either that the wave is reflected at the beginning of the beach, or at its end, a time interval for when the reflection reaches the probes can be found (vertical black lines in Fig. 8).

It can be seen in Fig. 8 that the average value of the free-surface elevation envelope, on a cross-section with constant x, follows the theoretical envelope found for a 2D wave and reaches a steady state, until reflection arrives. The time instant at which the reflection reaches the probes is defined as the time when the average envelope deviates by more than 1% of its steady-state value. The time window (grey area in Fig. 8) is then cut to ensure that its duration is a multiple of the wave period. The basic harmonic component amplitude is then found from a Fourier transform on this interval.

4. Description of inhomogeneity patterns

4.1. Description of the measurements results

Results from the Ocean basin tests of Rabliås and Kristiansen (2022) are provided in Fig. 9, for three wave periods, and with a wave steepness of $H/\lambda \approx 1/40$. The deviation of the measured wave elevations and target are in general within $\pm 20\%$. For $T \geq 1.5$ s, two main interference patterns seem to appear, on each side of the basin. They seem to follow similar patterns as interferences between a long-crested and a circular wave coming from either side.

Let $\underline{X}_0 = (x_0, y_0)^T$ be a given point, and $r = \|\underline{X} - \underline{X}_0\|$ the distance of any point $\underline{X}$ to it. Let $\eta_1(\underline{X}) = A_1 e^{ik_0(x-x_0)}$ be a long-crested wave system, and $\eta_2(\underline{X}) = a_2(r)e^{i(k_0 r+\alpha_0)}$ be a circular wave system originating from a source at $\underline{X}_0$, with α_0 being some initial phase difference.

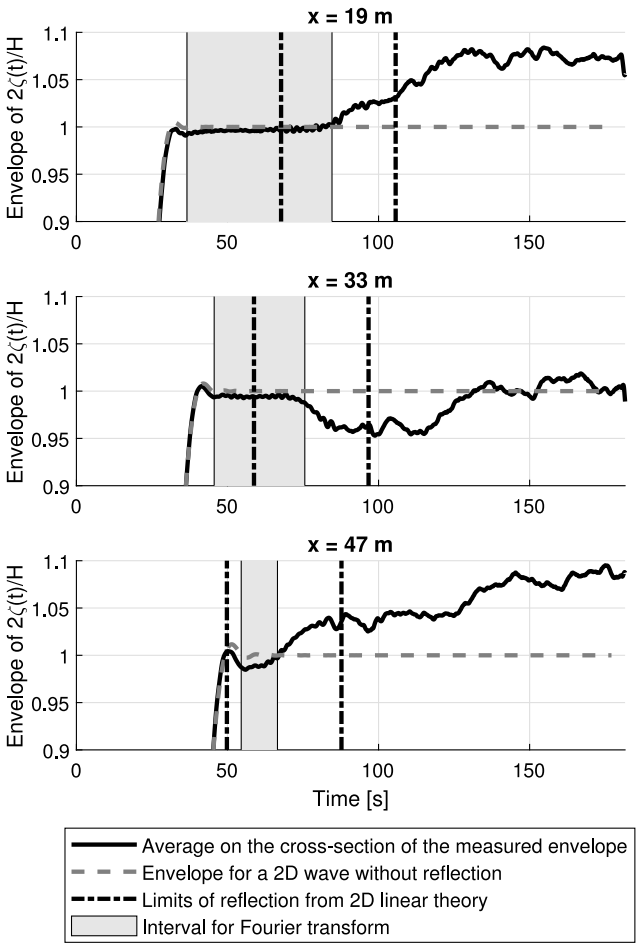

Fig. 8. Time series of the average envelope of the free-surface elevation across three cross-sections of the basin, for the experiments from Rabliås and Kristiansen (2022) in SINTEF's Ocean basin. Waves generated by a single flap wavemaker at $x = 0$ m, $T = 2$ s.

The lines of constructive interferences between those two wave systems then follow parabolas defined by $\tilde{x}_n = \left(\tilde{y}^2 - \alpha_n^2\right) / \left(2\alpha_n\right)$, where $\alpha_n = \alpha_0 + 2n\pi$, and $\underline{\tilde{X}} = k_0(\underline{X} - \underline{X}_0)$.

For large y (interference pattern 1 in Fig. 9), constructive interferences coincide with the patterns obtained with a source placed at the end of the partial wall before the BM3-beach, at ($x = 9.3$ m, $y = 48.6$ m). Its cause is the absorption by the BM3-beach, as will be demonstrated in Section 4.3. For small y (interference pattern 2 in Fig. 9), they coincide with a pattern for a source at ($x = 1.44$ m, $y = 0.24$ m). This is explained by a gap between the wavemaker and the side wall, as will also be demonstrated in Section 4.3. For $T = 1$ s, no clear pattern emerges. For this period, $\lambda = 1.56$ m, which is smaller than the distance between two wave probes. As the oscillations in wave amplitude seem to have a characteristic length around that of a wavelength, this would explain why it is difficult to see any clear pattern for this period.

Although the deviation can be up to more than 20%, the deviations are in general smaller – typically lower than 10% – within the usual working area used in model testing of floating structures (black rectangle in Fig. 9).

4.2. Comparison between experiments and numerical model

Deviations to the target amplitude found experimentally and numerically are next compared. Figs. 10 and 11 present the results across the whole basin, as well as along three transversal lines, for $T = 1.5$ s and $T = 2$ s. In order to show the convergence of the method, results

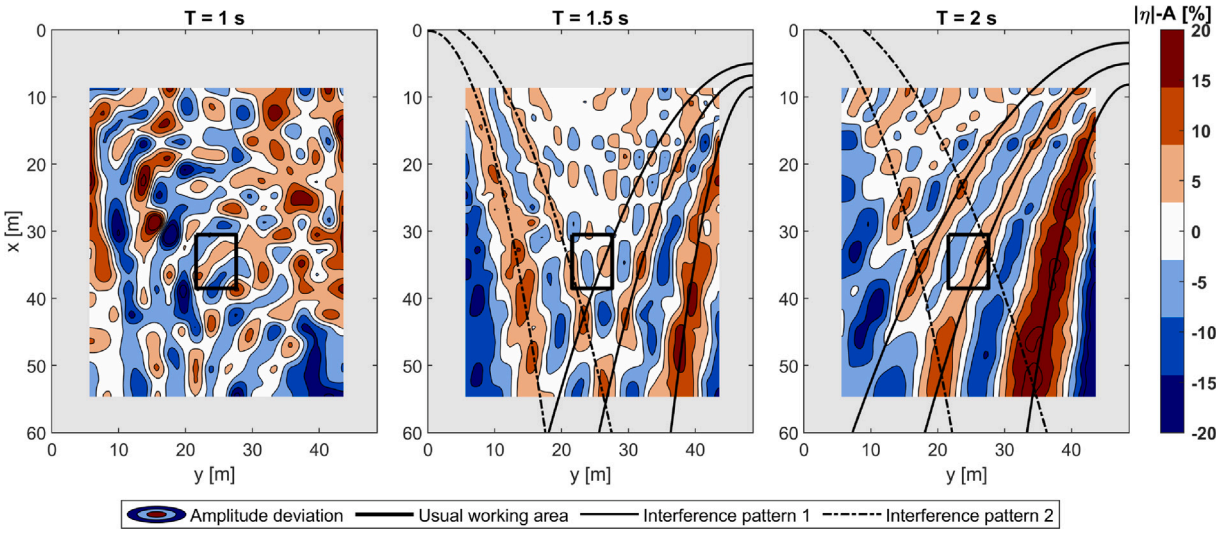

Fig. 9. Measurements of the deviation from the target amplitude of free-surface elevation for the experiments from Rabliås and Kristiansen (2022) in SINTEF's Ocean basin for waves generated by a single flap wavemaker at $x = 0$ m, and first lines of constructive interferences between a long-crested and a circular wave for a source at ($x_0 = 9.3$ m, $y_0 = 48.6$ m) for the first interference pattern and at ($x_0 = 1.44$ m, $y_0 = 0.24$ m) for the second.

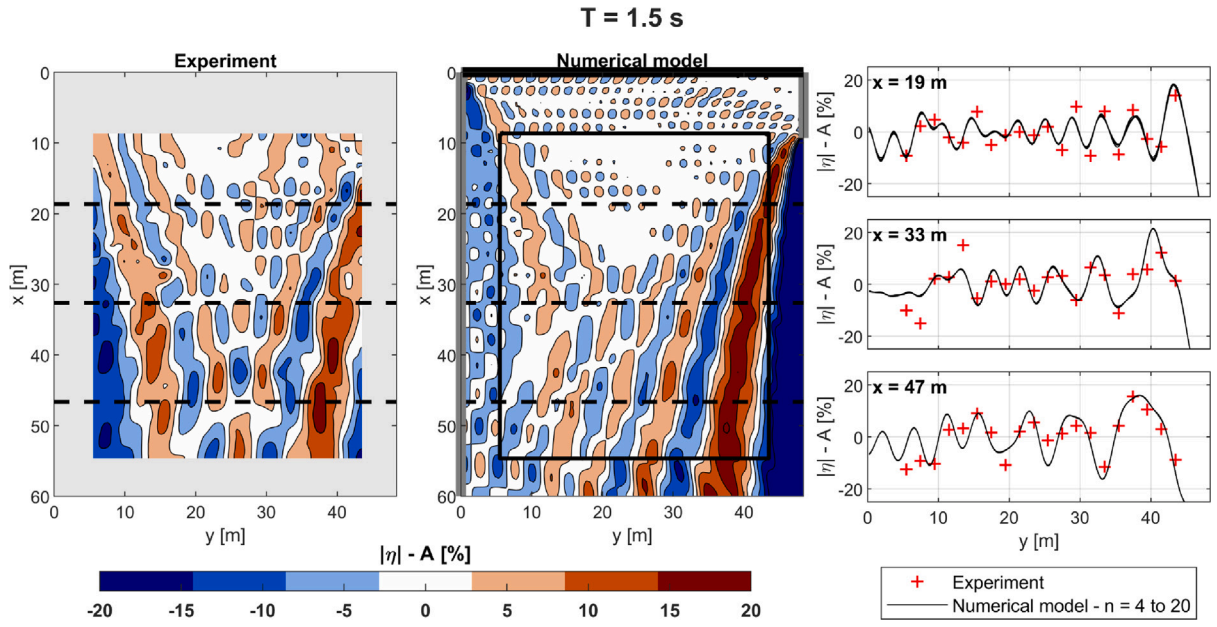

Fig. 10. Comparison of experimental and numerical results for a single panel BM2 wavemaker in deep water, and the described basin geometry (with walls represented by grey lines, and the wavemaker by a black line), for various mesh densities (characterized by the numbers of panels per wavelength, n) – $T = 1.5$ s – Gap of 0.24 m at $y = 0$ m.

for various mesh densities have been displayed simultaneously in the cross-section plots on the right-hand side of the figures. The number of panels is characterized by the number of panels per wavelength, n. 17 black curves show the results for values of n between 4 and 20. Consistent with the convergence study from Section 2.3.1, all curves are superposed, which means that, at $n = 4$, results have already converged. The further the cross-section is from the wavemaker, the faster the convergence is: this is also consistent with the assumptions behind the panel method.

It can be seen that the proposed model predicts well the experimental results, at least for the considered wave periods. For smaller wave periods, and especially near the wavemaker, small amplitude oscillations occur, which are not well captured by the probes array (as explained in the previous paragraph), and are also difficult to predict, as they can be influenced by small details of the basin's geometry. Among the unknowns that could explain the deviation are the exact behaviour of the BM3-beach. Waves are partially reflected by the beach, due to both its finite length, and the presence of vertical walls in the middle of the beach (indicated as supporting walls in Fig. 7). Perforated grids in front of the wall that precedes the BM3-beach (defined in Fig. 7) also absorb a fraction of the energy from the waves, while it is modelled as a rigid wall in the present model.

4.3. Sources of inhomogeneities

In order to find out which geometrical features of the basin influence the inhomogeneity patterns, results sensitivity to geometrical details of the basin was investigated through the following cases (see Fig. 12):

(a) For a basin with one of the lateral sides occupied by a perfectly absorbing beach (on the right-hand side of Fig. 12.a), an

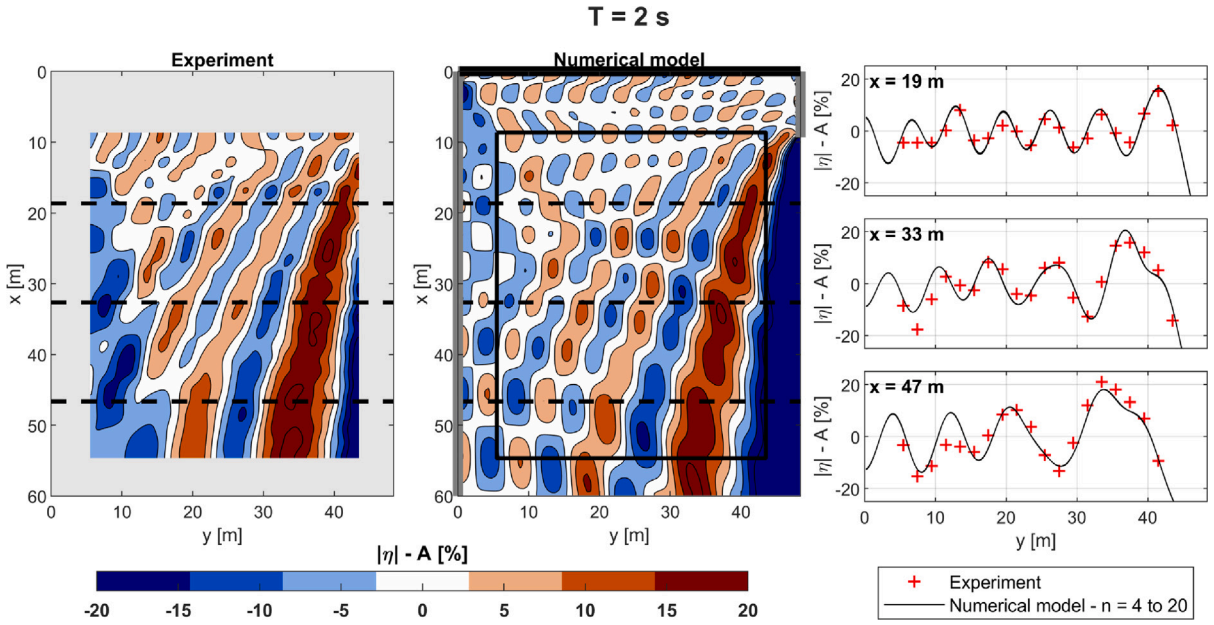

Fig. 11. Comparison of experimental and numerical results for a single panel BM2 wavemaker in deep water, and the described basin geometry (with walls represented by grey lines, and the wavemaker by a black line), for various mesh densities (characterized by the numbers of panels per wavelength, n) – $T = 2$ s – Gap of 0.24 m at $y = 0$ m.

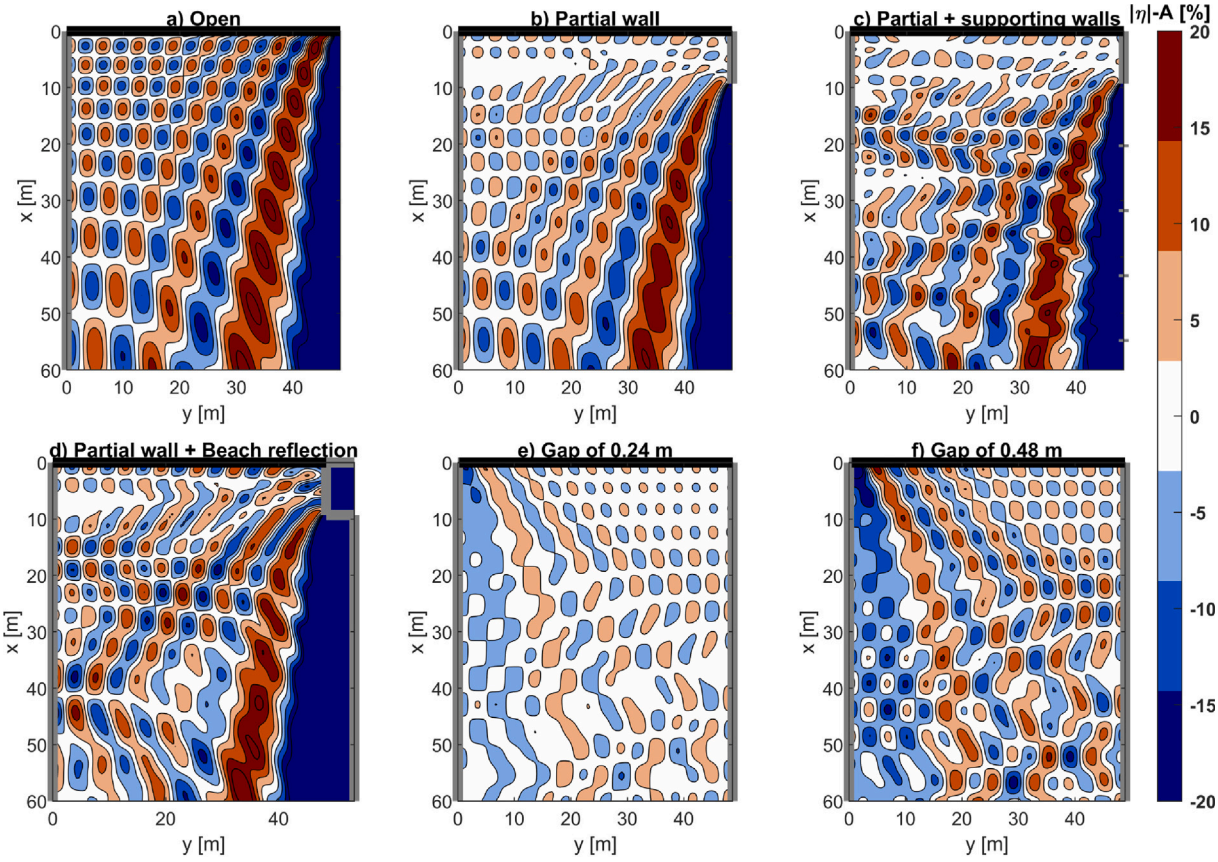

Fig. 12. Amplitude of free-surface elevation obtained by the numerical model for a single panel BM2 wavemaker in deep water and different basin geometries (with walls represented by grey lines, and the wavemaker by a black line) – $T = 2$ s.

interference pattern appears, similar to the one observed in the previous section, with deviations of up to and above ±25%. The root mean square of deviations in the usual working area is 8.3%. In reality, even between the columns, the BM3-beach does not completely absorb the incident waves. However, the absorption by the beach is what creates here the interference pattern. Adding partial reflection from the beach can potentially decrease the deviations from the target amplitude to a limited extent.

(b) Adding a partial wall before the BM3-beach shifts the interference pattern of a distance equal to its length. It also reduces the deviation levels slightly, but with otherwise minimal change.

(c) Adding the supporting walls has only a minor effect on the inhomogeneity pattern: it makes the interference pattern more complex, without significantly changing the maximum deviation with respect to the target amplitude. Here, interactions between reflections on the columns and on the beach are not considered.

(d) Adding partial reflection ($R = 30\%$) from the end of the BM3-beach at $y = 53.4$ m has even less effect on the pattern.

(e,f) Considering a basin with two infinite walls, but a gap between the wavemaker and one of the side walls (on the left-hand side of Fig. 12, see also Fig. 7), another interference pattern appears, similar to the one for an absorbing side beach, but with a lower deviation amplitude. Results are highly sensitive to the length of the gap. For a gap of only 0.24 m (actual value measured in the basin), the deviation from the target amplitude can be locally around 8%. Doubling the gap size, the deviation pattern can be seen for all wave periods, with deviations from the target amplitude up to 15%.

The dominant cause of inhomogeneity here is the discontinuity in the boundary on either side of the wavemaker, that is either the beach (modelled by an open boundary condition) or the gap.

4.4. Sensitivity to the gap size

The sensitivity of wave quality to the gap size was investigated more extensively. It was assumed here that the gap was directly beside the wavemaker, at $x = 0$ m. The goal here is to isolate the effect of the gap on inhomogeneities. However, the choice of boundary condition on the right side of the basin affects the results (with a gap on the left side and a wavemaker on the top side as in Fig. 12.e–f). One way of avoiding any perturbation from the right side is to put it at infinity: the problem is then that of an infinitely wide basin and wavemaker in the $y+$ direction, but with a gap between the wall at $y = 0$ m and the wavemaker. For an Ocean basin with a beach on the right side, this case is indeed representative of the influence of the gap only. However, it is not representative of the case of a basin with walls on both sides. Thus, two cases were looked at: respectively an infinitely wide wavemaker, and a wall as the right side boundary condition. The wave field in both cases can be solved analytically. For the first case, the solution for a finite wavemaker the width of the gap, as obtained in Section 2.3.2, is subtracted from the solution for a homogeneous regular wave. For the second case, the solution is directly that of Dalrymple (1989).

Two quantities of interest were chosen: the root mean square of the deviations from target amplitude (in percentage) in all the points of two areas, respectively a large area corresponding to that mapped in the first test campaign (see Figs. 9–11), and the usual working area (black rectangle in Fig. 9). Results for varying gap size and several wave periods are provided in Fig. 13. Results for the two walls and gap sizes of 0.24 m and 0.48 m correspond to the wave fields in Figs. 12.e and f respectively. For $T = 1$ s and the basin with two walls, deviations are much larger than for any other case. Indeed, as the basin studied is 48.4 m wide, for $T = 1$ s, the width of the basin is a multiple of the wavelength. As no damping was included, and steady state was assumed, in this case, there is resonance for one of the transversal modes of the basin. In reality, unlike for the other interference patterns, such resonance would take time to build up, and damping would limit the resonance.

It can be seen that in all cases, inhomogeneities are larger with two walls. This can be easily explained. A gap can be seen as a missing flap on the wavemaker. The deviations come from the interference between a long-crested and a missing wave, corresponding to that which the missing flap would have generated. With two walls, this missing wave is reflected by the wall on the right side, adding to the diffraction pattern.

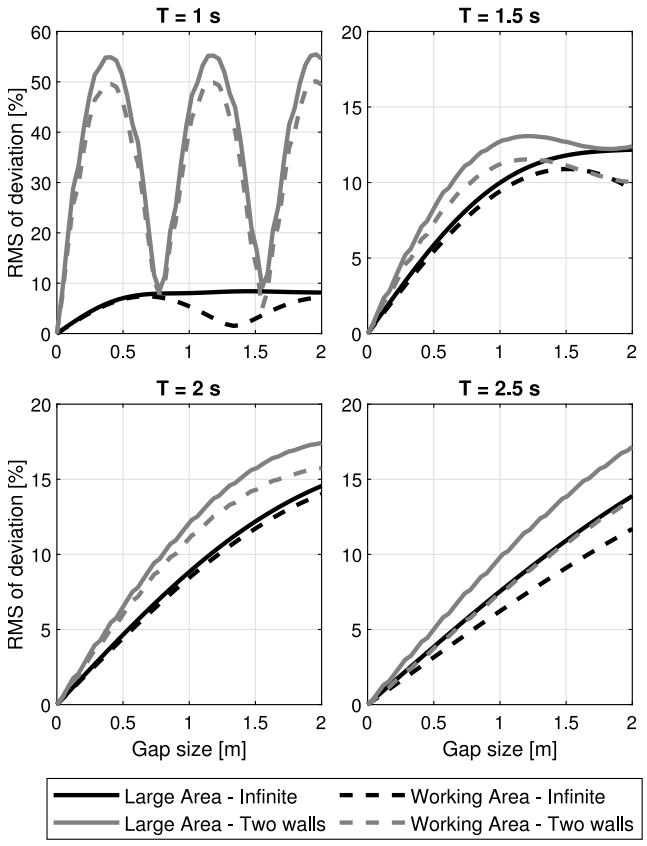

Fig. 13. Root mean square of deviations from target amplitude in a large area and in the usual working area, as a function of the gap size, for an infinitely wide basin, and for a basin with a wall on each side.

As expected, the results confirm the high sensitivity to the gap size. At $T = 2$ s and for both cases, when the gap size is above 1 m, the RMS of deviations in the working area becomes larger than what was obtained for the perfectly absorbing beach (Fig. 12.a).

5. Correction of inhomogeneities

5.1. Optimization method

Considering a multiflap wavemaker, deriving a correction to improve the uniformity of waves in a given area of the basin is an optimization problem. In it, the variables are the complex amplitudes of the displacement of each flap, $X_{a,n}$ for $n \in [\![1, N]\!]$, and the goal function is some measure of the quality of the generated wave field. As linear potential flow theory is used, it is possible to first find the wave field generated by each flap independently, and then obtain the set of possible wave fields by summing those elementary solutions.

Using elementary wave fields for optimization of the wave generation is not restricted to this panel method: any other approach for generating the basis functions could be used, for which the underlying theory is linear (for instance spectral methods). A disadvantage is that optimization methods are often black boxes, and hence will probably give less theoretical insight into the limitations of a given basin than if an analytical solution was directly derived for the optimal flap motion. However, analytical solutions are restricted to simple basin geometries, and cannot be presently used.

The function to be minimized is chosen to be the difference between estimated and target complex free-surface elevation on an arbitrary number of points. A standard least square method is then used. The optimization is done under constraints being the physical limitations of the flaps in terms of angle and velocity.

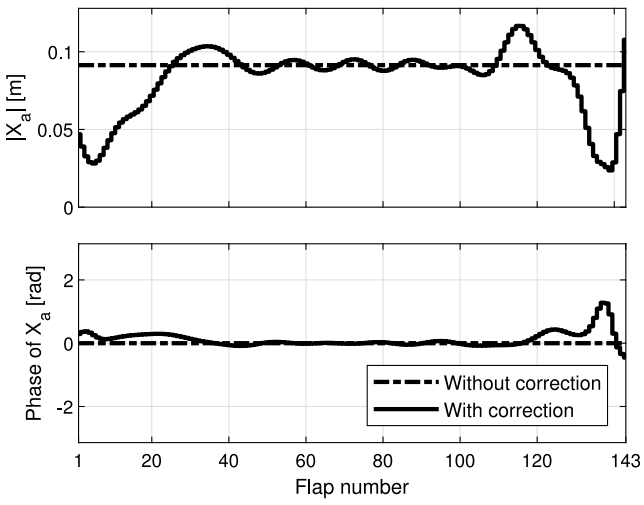

Fig. 14. Example of amplitude and phase of each flap displacement with and without correction – Small steepness wave ($H/\lambda = 1/45$) of period $T = 2$ s generated by the multiflap wavemaker BM3 – Optimization area depicted in Fig. 15.

The method relies on specified complex amplitudes of waves at various locations. If the chosen points are too sparse (more than a few wavelengths between them), or if they do not cover the whole extent of the basin, the optimization could lead to the appearance of high amplitude components either between them or on the sides of the optimization area. Assuming linear theory, such high amplitude components might theoretically help improve the quality of the results. However, in practice, higher amplitude means getting further from the assumptions of linear theory, or could even lead to breaking waves. Thus, the uncertainties they bring usually exceed the potential gains. To prevent the apparition of those components, or at least control them, a weight on the flap displacement variance, $\frac{c}{N}\sum_{n=1}^{N}|X_{a,n}|^2$, can be added to the goal function. Its constant, c, should be calibrated in order to remove the unwanted components, while not altering the desired wave field.

The optimization problem in itself is relatively simple, and a simple gradient descent has proven efficient. It was compared to the MATLAB® function *fmincon* (MATLAB, 2022), which uses an interior-point method, with similar results.

In the present work, the optimization was conducted on an array of 50×30 points distributed evenly in a centred area of the basin (black rectangle in Fig. 15). All points from the array had the same weight in the calculation of the RMS. The weight on the flap displacement amplitudes was taken as $c = 0.05$.

5.2. Results for low steepness regular waves

The goal of the second experimental campaign described in Section 3.2 and carried out in 2022 was to test the efficiency of the correction, with waves from a multiflap wavemaker. For the case without correction, all flaps move synchronously with an amplitude found directly from the transfer functions obtained by Biésel and Suquet (1951) within the assumption of two-dimensional wave propagation. For the correction, the optimization method previously described was applied to find the complex flap displacement amplitudes. An example of result from the optimization is presented in Fig. 14.

Results from experiments with and without correction are compared in Fig. 15, for two wave periods, and waves propagating perpendicularly from the multiflap wavemaker ("BM3" in Fig. 7). The colours indicate deviation from the target amplitude, and the arrows represent local mean wave direction, as the inhomogeneity in fact includes a short-crested wave system. Local direction is here defined as the mean

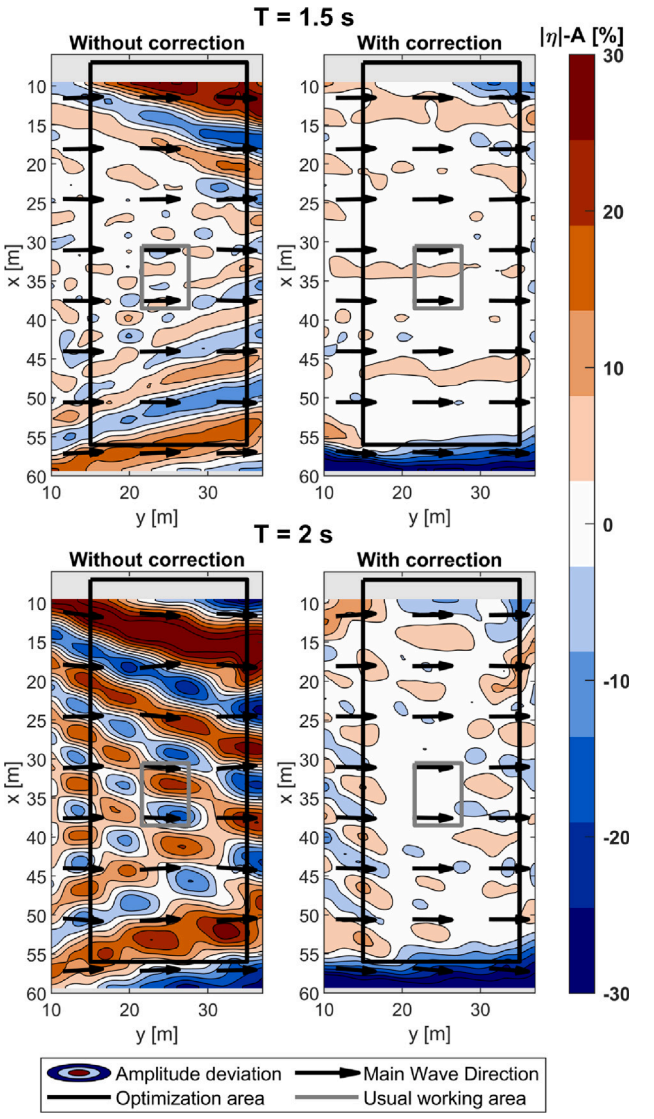

Fig. 15. Experimental results for deviation from target amplitude with and without correction, for a small steepness wave ($H/\lambda = 1/45$), and waves generated by a multiflap wavemaker at $y = 0$ m.

direction of the slope of the waves, found from the circular array. For small steepness waves ($H/\lambda = 1/45$), and without correction, patterns of deviation appear once again on both sides of the basin.

The pattern on the bottom side is created by the BM2-beach. The deviations of up to 18% for $T = 1.5$ s and up to 25% for $T = 2$ s correspond to what was discussed in Section 4.3 for a perfectly absorbing beach on the side of the wavemaker. The pattern on the top side is created by a large gap 1.44 m wide at $x = 0$ m. Inhomogeneities created by this gap are larger than for a perfectly absorbing beach, reaching close to 30% for $T = 1.5$ s and more than 35% for $T = 2$ s, with large deviations extending to the usual working area in the centre of the basin (grey rectangle in Fig. 15). This is coherent with the observations made in Section 4.4, as the gap is larger than 1 m.

Applying the correction efficiently reduces inhomogeneities in both optimization and usual working areas. For a regular wave of $T = 1.5$ s, the deviations which were up to 30% are decreased to below 6%. For $T = 2$ s, likewise, they go from more than 35% to less than 10%. The remaining deviations here are not present in the numerical model: they do not originate from physical constraints of the wave generation but from discrepancies between the numerical model and the experiments,

Table 3
RMS of deviations from target amplitude (in percentage) for all probes in the optimization or the usual working areas, as observed in experiments for low steepness regular waves ($H/\lambda = 1/45$), and waves generated by a multiflap wavemaker at $y = 0$ m.

T [s]	Correction	Optimization area	Working area
1.5	Without	9.2	4.1
1.5	With	2.8	2.1
2	Without	15.2	11.9
2	With	3.7	1.3

presented in Section 4.2. The root mean square of deviations on all probes for both the optimization and the usual working area are presented in Table 3.

On the sides of the optimization area, as expected, waves have lower amplitudes. This is due to the weight on flap displacement variance added to the goal function in the optimization problem. Accordingly, flap displacement amplitudes mainly decrease around both extremities of the wavemaker.

5.3. Simplified correction method

To assess how important it is to take into account details of the basin geometry, another correction was implemented: the one adapted to a finite length wavemaker in an infinite basin (or equivalently with wave absorbers on both side of the wavemaker), without partial side walls. This corresponds to the specific case studied by Matsumoto and Hanzawa (1996). The efficiency of this correction was compared to the one presented in this work (with complex basin geometry). This study was restricted to a few locations in the basin only. Results from experiments with both corrections are compared in Fig. 16, for the same wave periods and steepnesses as in Section 5.2. For the shortest wave, slightly larger deviations appear in one of the corners of the basin. It is for longer waves that the usefulness of the new correction can clearly be seen, with deviations on the top right corner of less than 8% with the new correction, versus up to around 15% with the other one (see Fig. 16).

In both cases, the simple correction assuming an infinite basin still helps improving homogeneity. Indeed, with the optimization method described in Section 5.1, waves are generated that propagate mainly towards the optimization area (black rectangles in Fig. 16). This area does not extend all the way to the sides of the basin, so that, with a weight on flap displacement variance, the wave amplitude on the sides of the optimization area is much lower than inside it. Thus, the waves interacting with the boundaries carry much less energy than if no correction was applied. This means that if the boundaries of the basin are far enough from the optimization area, applying a correction will reduce inhomogeneities, even with a poor description of the boundaries. This explains why both correction help, even though the one taking into account details of the basin geometry is more efficient.

5.4. Influence of wave steepness

The correction was also tested with steeper waves, $H/\lambda = 1/20$. Without correction, and for both wave periods, the same patterns of deviation as for the small steepness waves appear (see Fig. 17). The deviations are interestingly slightly less important (from a maximum value of more than 35% in the upper-right corner at $T = 2$ s for the small steepness wave, to 23% for the steeper wave). A non-linear model would be needed to possibly explain the change in differences due to the increase of wave steepness.

With correction, deviations from the target amplitude are reduced to values close to those observed for the lesser steepness: the correction seems to still be efficient, something which has importance in practice.

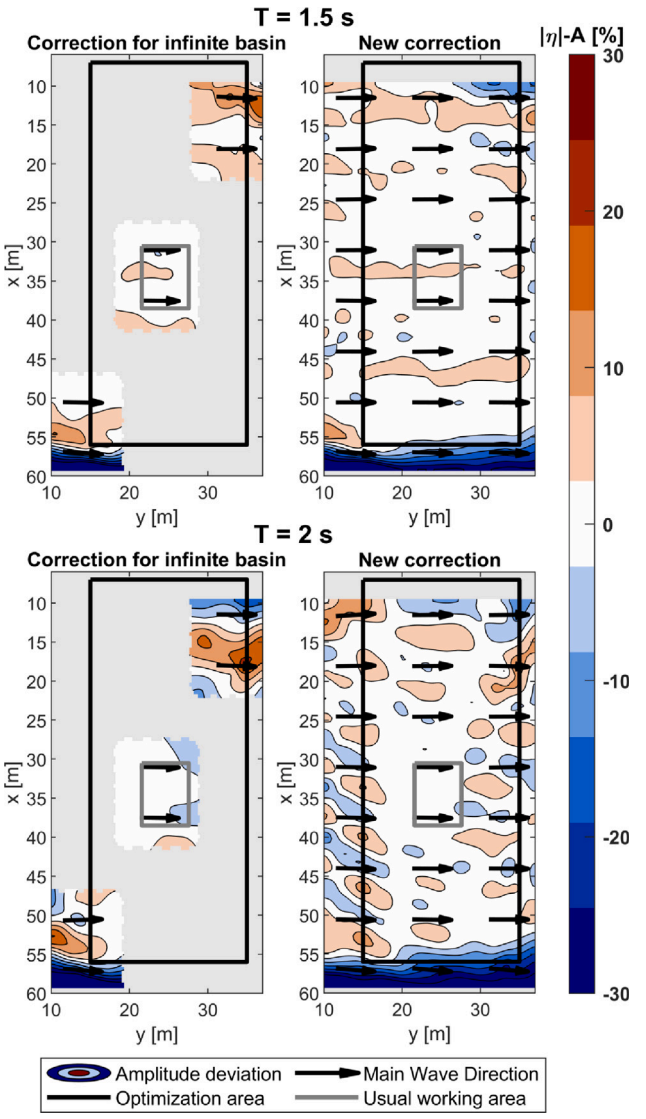

Fig. 16. Experimental results for deviation from target amplitude with two different corrections (already existing correction for a basin with wave absorbers on both sides, and the one developed in the present article, for the actual basin geometry), for a small steepness wave.

6. Consequences of inhomogeneities

In order to provide quantitative examples of how inhomogeneities can affect model tests, two cases are presented in this section, and studied numerically, assuming linear theory. The first case is the effect of inhomogeneities on the energy spectrum observed in a given location. The second is the linear wave excitation loads on a structure, affected both by the spatial variations of wave amplitudes, and by changes in wave direction.

6.1. Irregular waves

The model presented here is linear, and regular waves have been investigated. However, assuming linearity, results obtained for the impact of imperfect basin boundaries on wave homogeneity can be applied directly to irregular waves. By performing simulations for various periods at a fixed location in the basin, a transfer function can be obtained, that allows finding the wave spectrum as a function of a target spectrum. This is exemplified for one spatial point in Fig. 18. Consistent with what

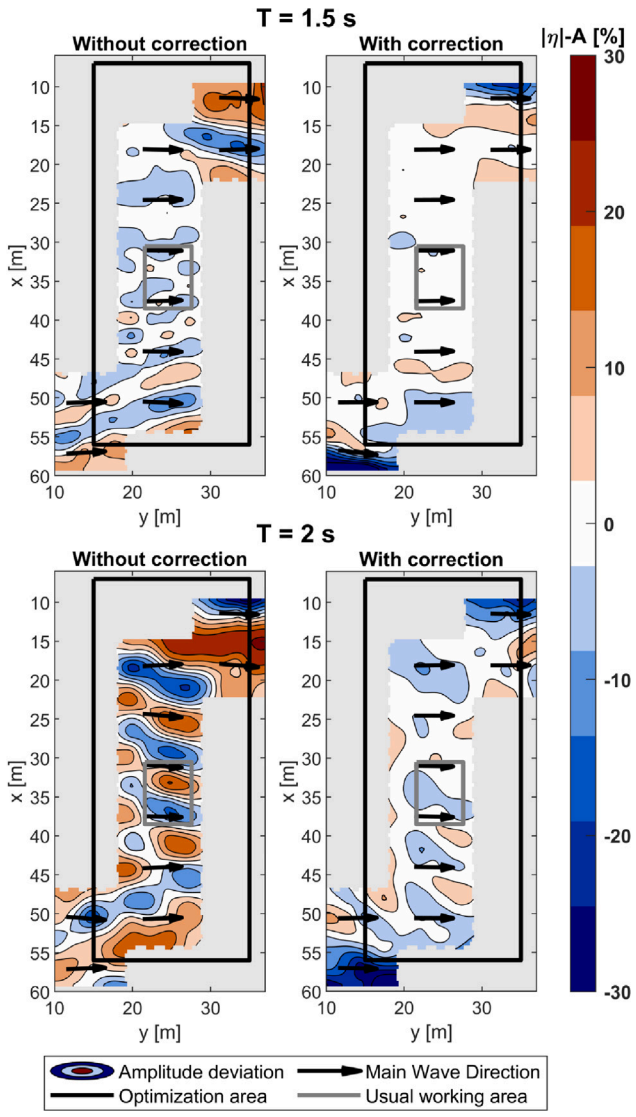

Fig. 17. Experimental results for deviation from target amplitude with and without correction, for a steeper wave ($H/\lambda = 1/20$), and waves generated by a multiflap wavemaker at $y = 0$ m.

our previous discussions have indicated, deviations increase with the period.

The frequency-dependent deviations from the theoretical wave spectrum is similar to what is seen in practice in experiments, at least before calibration (see Fig. 19). It also looks similar to a random realization of a spectrum, obtained by drawing amplitudes from a Rayleigh distribution (Tucker et al., 1984). The contribution from inhomogeneities can be difficult to isolate from that of randomness from a single measurement. However, the deviation caused by inhomogeneities is constant across realizations: it is a deviation of the expected value of the amplitudes.

In addition to affecting the amplitudes of the waves, inhomogeneities also modify the main direction of the waves. On the contrary, drawing random amplitudes for a long-crested wave has no effect on the wave direction. Even with a single experiment – that is a single realization of a spectrum for a long-crested wave – deviations in the main direction of the waves indicate inhomogeneities.

In irregular waves, calibration is traditionally applied from measurements in a single location, to ensure that the measured wave

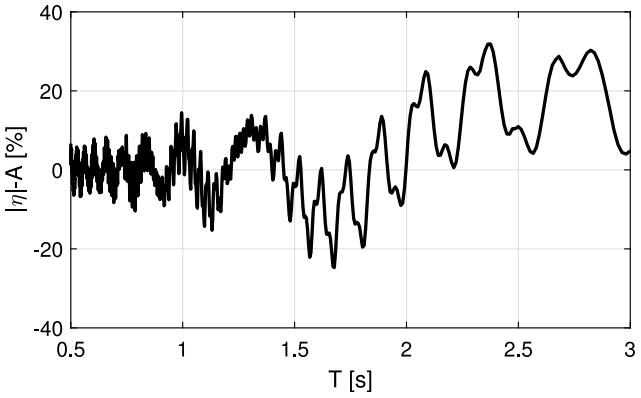

Fig. 18. Example of transfer function between target and obtained wave spectrum. Fixed point ($x = 50$ m, $y = 25$ m), and waves from BM3 without correction.

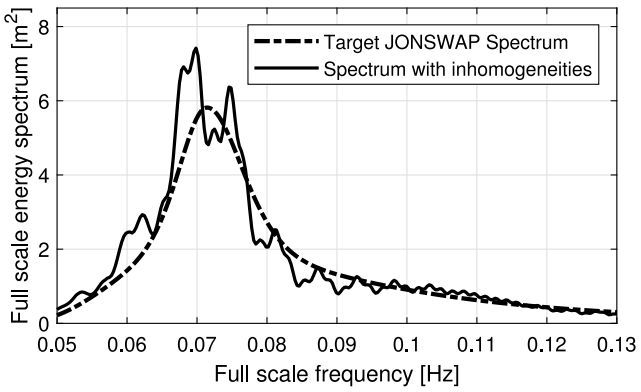

Fig. 19. Example of application of the transfer function from Fig. 18 on a JONSWAP spectrum – $T_P = 14$ s, $H_S = 10$ m, scale 1:50.

spectrum matches the target. However, without correction of inhomogeneities, it is only locally that this type of calibration improves wave quality. For each wave period, it moves the whole pattern of amplitudes in the basin up or down so that the deviation from target amplitude reaches zero on the calibration point. Thus, it can even worsen the maximum deviation caused by inhomogeneities over the whole basin. When applying a correction, calibration can still be used as usual. It will then theoretically improve wave quality over the whole area of optimization. By already removing deviations caused by inhomogeneities, it could even lead to a better first attempt in the calibration process, thus resulting in faster convergence. However, this would require experimental validation that was not done in the present article.

6.2. Linear wave excitation loads on a structure

In order to provide a quantitative example of how inhomogeneities can affect wave loads on structures, the linear Froude–Krylov loads were computed for an example case: two rigidly connected vertical truncated cylinders, of dimensions small compared to the wavelengths (see Figs. 20 and 21), placed in the middle of the basin. The wave field was derived with our numerical method, and with the same basin geometry as in the second test campaign, without correction.

For small structures for which the long wave approximation can be used, the amplitude of the linear Froude–Krylov loads is proportional to the linear wave amplitude at the centre of the body. Thus, the transfer function derived here-above (see Fig. 18) can be directly used to find the deviation in the amplitude of the force.

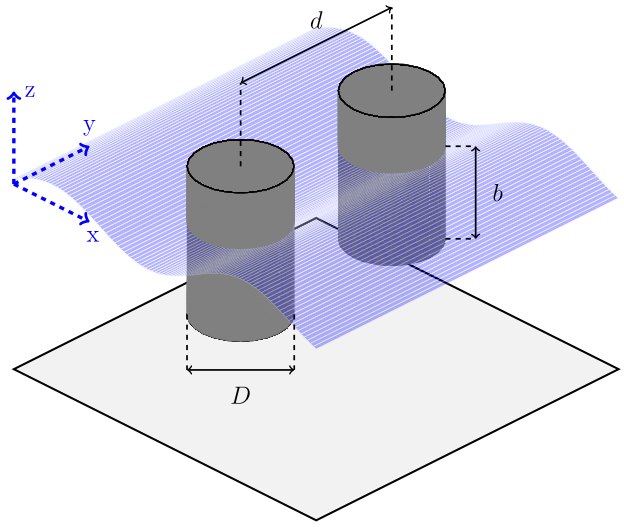

Fig. 20. Definition of the dimensions for the pair of cylinders considered.

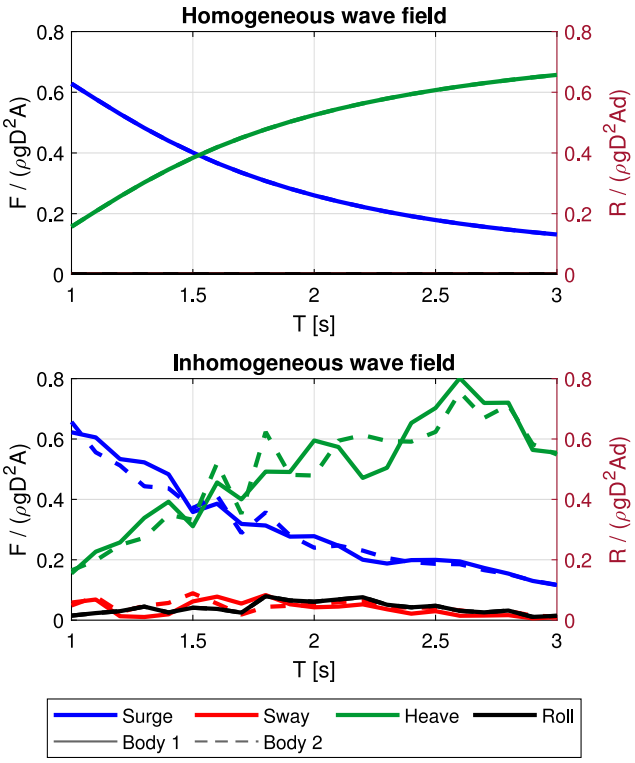

Fig. 21. Example result from the presently developed model – Dimensionless Froude–Krylov force for two cylinders in the middle of the basin – $D = 20$ m, $b = 20$ m, $d = 60$ m, Scale 1:50.

However, in addition to wave amplitude variations, inhomogeneities also imply variations in the main wave direction. And as the horizontal Froude–Krylov load is aligned with the particle acceleration, this also means that wave excitation loads in sway can appear, even with a nominally incident long-crested wave (see Fig. 21). For larger structures, a semi-submersible for instance, differences between the heave excitation of the various columns and pontoons will also cause unexpected roll moments (see Figs. 20 and 21).

With only a linear wave model, except in specific cases, non-linearities in forces cannot be accounted for. However, the order of magnitude of deviations at second order is around the square of the first order deviations, so that 20% deviation for the linear component of the wave would mean around 40% deviation on second-order loads. For responses associated with steep irregular wave events, such as wave run-up on vertical columns, higher than second-order effects matter. However, because such an event involves several wave frequencies, one may expect that the effect of inhomogeneity cancels to some extent, as shown in Figs. 18 and 19. This requires dedicated further studies.

7. Conclusion

The sensitivity of wave field homogeneity to geometrical details of hydrodynamic facilities was investigated for SINTEF's Ocean Basin. It seems that two main elements explain a large part of the observed deviation for long-crested waves: the presence of a beach on one side of the basin, and the gap between the wavemaker and the wall on the other side. Results are highly sensitive to variations of the gap width, a few tens of centimetres being enough to induce deviations of amplitude up to $\pm 10\%$ in the whole basin. Those inhomogeneities might not affect experiments run on a small centred working area in the basin. However, they would matter for arrays or large structures, if not corrected.

An efficient method for predicting the wave generated by a multiflap wavemaker with linear theory and constant water depth has been presented and compared to experiments. It was used to derive a correction method for improving spatial uniformity of waves, and thus to extend the working area in a basin. This correction method was experimentally tested for regular waves. It proved to be efficient even with steepnesses at least up to $H/\lambda = 1/20$. Small variations were observed in the amplitude of the inhomogeneity patterns when increasing the steepness. As a further work, a non-linear model should then be developed to understand their cause, and maybe extend the validity of the correction to even larger steepness than those that could be tested with the wavemaker that was used. This would also allow for a better understanding of how much wave inhomogeneity affects higher-order phenomena and responses of structures.

Even though the optimization method developed here was only tested for regular waves, it could be applied to irregular and short-crested sea states. Validation should then be performed for those cases. However, all the effects described in the present work appear before reflection. In reality, and especially for experiments with irregular waves where long time series are needed, because of the reflection from the wave absorbers, standing waves will appear, that will also be inhomogeneous. Directional reflection from wave absorbers should then also be looked at and included in the model.

Even though the numerical model presented here was only validated for an Ocean basin, the method developed here theoretically applies to any wave basin of constant depth. However, for tanks that do not have a multiflap wavemaker, the model can only predict possible inhomogeneities, but not correct them. This is often the case for wave flumes, and also sometimes for towing tanks. For tanks for which depth varies in space, for instance tanks having a bottom with steps, the current model cannot be used. Further work could expand the formulation in order to also include sudden depth variations in the basin. An approach could be, for instance, to separate the domain into several subregions of constant depth, and apply matching conditions at their boundaries.

The optimization method developed here can be used for any target sea state, and not only long-crested or homogeneous waves. It would then be possible to use such a model in order to generate realistic inhomogeneous coastal waves in a basin, as long as the effects of changes in bathymetry are negligible locally around the tested structure.

CRediT authorship contribution statement

Sébastien Laflèche: Conceptualization, Methodology, Software, Validation, Formal analysis, Investigation, Writing – original draft. **Babak Ommani:** Conceptualization, Supervision, Writing – review & editing. **Trygve Kristiansen:** Conceptualization, Resources, Writing – review & editing. **Sébastien Fouques:** Conceptualization, Writing – review & editing.

Declaration of competing interest

The authors declare that they have no known competing financial interests or personal relationships that could have appeared to influence the work reported in this paper.

Data availability

Upon request, the authors will evaluate sharing the data together with other parties sharing the data ownership.

Acknowledgements

This work was partly supported by the Research Council of Norway through SFI BLUES, grant number 309281. The authors are also grateful to the Research Council of Norway for the grant provided under the FORINFRA Program (Large Scale Infrastructures), Phase III, grant 269870, and to Rabliås and Kristiansen for making available the data from their test campaign of 2018.

References

Abramowitz, M., Stegun, I.A., 1964. Handbook of mathematical functions with formulas, graphs, and mathematical tables, ninth Dover printing, tenth GPO printing In: Applied Mathematics Series, Vol. 55, U.S. Department of Commerce, National Bureau of Standards, p. 369.

Barailler, L., Gaillard, P., 1967. Évolution récente des modèles mathématiques d'agitation due à la houle. Calcul de la diffraction en profondeur non uniforme. Houille Blanche 53, 861–870. http://dx.doi.org/10.1051/lhb/1967060.

Biésel, F., Suquet, F., 1951. Les Appareils générateurs de houle en laboratoire. Houille Blanche (2), 147–165. http://dx.doi.org/10.1051/lhb/1951033.

Cheng, Z., Gao, Z., Moan, T., 2018. Hydrodynamic load modeling and analysis of a floating bridge in homogeneous wave conditions. Mar. Struct. 59, 122–141. http://dx.doi.org/10.1016/j.marstruc.2018.01.007.

Dai, J., Leira, B.J., Moan, T., Alsos, H.S., 2021. Effect of wave inhomogeneity on fatigue damage of mooring lines of a side-anchored floating bridge. Ocean Eng. 219, 108–304. http://dx.doi.org/10.1016/j.oceaneng.2020.108304.

Dalrymple, R.A., 1989. Directional wavemaker theory with sidewall reflection. J. Hydraul. Res. 27 (1), 23–34. http://dx.doi.org/10.1080/00221688909499241.

Gilbert, G., Huntington, S.W., 1991. A technique for the generation of short crested waves in wave basins. J. Hydraul. Res. 29 (6), 789–799. http://dx.doi.org/10.1080/00221689109498959.

MacCamy, R.C., Fuchs, R.A., 1954. Wave forces on piles: A diffraction theory. Technical Memorandum 69, US Army Corps of Engineers Beach Erosion Board, Washington DC, USA, p. 22.

MATLAB, 2022. Version 9.12.0 (R2022a). The MathWorks Inc., Natick, Massachusetts.

Matsumoto, A., Hanzawa, M., 1996. New optimization method for paddle motion of multi-directional wavemaker. In: Coastal Engineering 1996. American Society of Civil Engineers, pp. 479–492. http://dx.doi.org/10.1061/9780784402429.038.

Mei, C.C., Stiassnie, M.A., Yue, D.K.-P., 2005. Theory and Applications of Ocean Surface Waves. In: Advanced Series on Ocean Engineering, Vol. 23, World Scientific, http://dx.doi.org/10.1142/5566.

Nishimura, H., Matsuoka, M., Matsumoto, A., 1994. A generalized green-function method for wave field analysis. In: Coastal Engineering. American Society of Civil Engineers, Kobe, Japan, pp. 442–454. http://dx.doi.org/10.1061/9780784400890.034.

O'Boyle, L., Elsäßer, B., Whittaker, T., 2017. Methods to enhance the performance of a 3D coastal wave basin. Ocean Eng. 135, 158–169. http://dx.doi.org/10.1016/j.oceaneng.2017.03.006.

O'Dea, J.F., Newman, J.N., 2007. Numerical studies of directional wavemaker performance. In: SNAME American Towing Tank Conference. Day 2 Thu, August 09, 2007, http://dx.doi.org/10.5957/ATTC-2007-002.

Ota, D., Houtani, H., Sawada, H., Taguchi, H., 2021. Optimization of segmented wavemaker control to generate spatially uniform regular waves in a rounded-rectangular wave basin. In: International Conference on Offshore Mechanics and Arctic Engineering. Volume 6: Ocean Engineering, http://dx.doi.org/10.1115/OMAE2021-62773.

Rabliås, Ø., Kristiansen, T., 2019. Free running maneuvering tests of the DTC hull in calm water and regular waves with focus on uncertainty analysis based on repetition tests. In: 5th MASHCON Proceedings. Ostend, Belgium, pp. 328–340.

Rabliås, Ø., Kristiansen, T., 2022. A rational model for maneuvering in irregular waves with the effect of waves on the propeller and rudder inflow taken into account. Ocean Eng. 243, 110–186. http://dx.doi.org/10.1016/j.oceaneng.2021.110186.

Rodrigues, J.M., 2021. A procedure to calculate first-order wave-structure interaction loads in wave farms and other multi-body structures subjected to inhomogeneous waves. Energies 14 (6), 1761. http://dx.doi.org/10.3390/en14061761.

Schäffer, H.A., 1996. Second-order wavemaker theory for irregular waves. Ocean Eng. 23 (1), 47–88. http://dx.doi.org/10.1016/0029-8018(95)00013-B.

Schäffer, H., Steenberg, C., 2003. Second-order wavemaker theory for multidirectional waves. Ocean Eng. 30 (10), 1203–1231. http://dx.doi.org/10.1016/S0029-8018(02)00100-2.

Sommerfeld, A., 1949. Partial differential equations in physics. In: Pure and Applied Mathematics, Vol. 1, Academic Press, pp. 232–235. http://dx.doi.org/10.1016/S0079-8169(08)60771-0.

Tucker, M., Challenor, P., Carter, D., 1984. Numerical simulation of a random sea: a common error and its effect upon wave group statistics. Appl. Ocean Res. 6 (2), 118–122. http://dx.doi.org/10.1016/0141-1187(84)90050-6.

WAMIT Inc., 2020. WAMIT - user manual. URL https://www.wamit.com/manual.htm.

Wilbraham, H., 1848. On a certain periodic function. Camb. Dublin Math. J. 3, 198–201.